ATLAS NOTE

ATLAS-CONF-2015-015

March 24, 2015

A search for $B - L$ R-parity-violating scalar top decays in $\sqrt{s} = 8$ TeV pp collisions with the ATLAS experiment

The ATLAS Collaboration

Abstract

A search is presented for direct scalar top pair production where the scalar tops decay via an R-parity-violating coupling to a final state with two leptons and two identified b-jets. The analysis uses 20.3 fb^{-1} of $\sqrt{s} = 8$ TeV proton-proton collision data collected with the ATLAS detector at the LHC. No significant excess is observed over the Standard Model background. Assuming a supersymmetric minimal $B - L$ extension to the Standard Model, limits on the scalar top mass are placed between 500 GeV and 1 TeV with a branching fraction above 20% for the scalar top to decay to an electron or a muon and a b-quark.

1 Introduction

The extension of the Standard Model of particle physics with supersymmetry (SUSY) [1–9] immediately leads to processes that violate both baryon number (B) and lepton number (L), leading to rapid proton decay and lepton-number-violating processes, such as unseen decays of $\mu \to e\gamma$, in conflict with experimental bounds. A conventional assumption to prevent these processes is to impose conservation of R-parity [10–14], defined as $R = (-1)^{3(B-L)+2s}$ where s is the spin of the particle. This has a value of $+1$ for Standard Model particles and -1 for SUSY particles. In this case SUSY particles are produced in pairs, and the lightest supersymmetric particle (LSP) is stable. Further, this stable LSP cannot carry electric charge or color charge without coming into conflict with astrophysical data. At the LHC, the conventional experimental signature for SUSY particles includes significant missing transverse momentum due to the non-interaction of the LSP with the detector.

An alternative approach is to add a local symmetry $U(1)_{B-L}$ to the $SU(3)_C \times SU(2)_L \times U(1)_Y$ Standard Model with right-handed neutrinos. The minimal supersymmetric extension then only needs a vacuum expectation value for a right-handed sneutrino in order to spontaneously break the $B - L$ symmetry [15–26]. This minimal $B - L$ model violates lepton number but not baryon number, and is consistent with proton stability and the bounds on lepton number violation. The LSP can now decay via R-parity-violating (RPV) processes, and may now carry color and electric charge. This leads to unique signatures [26–30] that are disallowed in conventional models with R-parity conservation. The case where the LSP is a scalar top (stop) is most interesting since, in general, the large mass of the top quark acts to make the lightest stop significantly lighter than the other squarks due to renormalization group effects [31, 32]. The stop decays via an RPV interaction to a charged lepton (of any flavor) and a b-quark. The decay branching fractions to eb, μb, and τb may be different in a manner related to the neutrino mass hierarchy [33, 34].

In this note, a search is presented for direct stop pair production, with the decay of each stop via an RPV interaction to a charged lepton (electron or muon) and a b-quark, as shown in Figure 1. The experimental signature is two oppositely charged leptons and two identified b-jets. The analysis considers $eebb$, $e\mu bb$, and $\mu\mu bb$ final states. Final states with taus are not considered for this search. The distinguishing features are two pairs, each of a lepton and a b-jet, with a resonance in the invariant mass distribution of each pair. In contrast to R-parity conserving searches, there is no significant missing transverse momentum.

Previous searches for lepto-quarks at ATLAS [35–38] and CMS [39–42] have considered pair production of first, second, and third generation lepto-quarks, but have not examined the signature of a resonance in the invariant mass of an electron and a b-jet or a muon and a b-jet. The results of these searches have already been interpreted to set limits on the stop mass and its decay branching fractions in the $B - L$ model [33, 34].

2 The ATLAS detector

The ATLAS experiment [43] is a multipurpose particle physics detector with a forward-backward symmetric cylindrical geometry and nearly 4π coverage in solid angle.[1] The inner tracking detector (ID)

[1] ATLAS uses a right-handed coordinate system with its origin at the nominal interaction point (IP) in the center of the detector and the z-axis along the beam pipe. The x-axis points from the IP to the center of the LHC ring, and the y-axis points upward. Cylindrical coordinates (r, ϕ) are used in the transverse plane, ϕ being the azimuthal angle around the beam pipe. The pseudorapidity is defined in terms of the polar θ angle as $\eta = -\ln[\tan(\theta/2)]$. The distance parameter (in η-ϕ space)

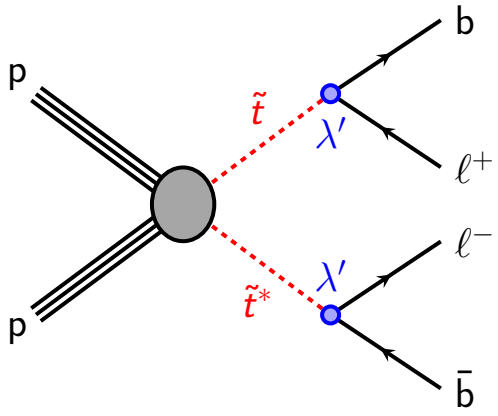

Figure 1: Simplified model of pair production of stops, each with an RPV decay to a charged lepton and b quark.

covers the pseudorapidity range $|\eta| < 2.5$, and consists of a silicon pixel detector, a silicon microstrip detector, and, for $|\eta| < 2.0$, a transition radiation tracker. The ID is surrounded by a thin superconducting solenoid providing a 2 T magnetic field. A high-granularity lead/liquid-argon (LAr) sampling electromagnetic calorimeter covers the region $|\eta| < 3.2$. A steel/scintillator-tile calorimeter provides hadronic coverage in the range $|\eta| < 1.7$. LAr technology is also used for the hadronic calorimeters in the end-cap region $1.5 < |\eta| < 3.2$ and for electromagnetic and hadronic measurements in the forward region up to $|\eta| = 4.9$. The muon spectrometer (MS) surrounds the calorimeters. It consists of three large air-core superconducting toroid magnet systems, precision tracking chambers providing accurate muon tracking out to $|\eta| = 2.7$, and additional detectors for triggering in the region $|\eta| < 2.4$.

3 Monte Carlo simulation samples

Monte Carlo (MC) simulation is used to estimate the detector response and efficiency to reconstruct the signal process, estimate systematic uncertainties, and to predict the backgrounds from Standard Model processes. The response of the detector is simulated using a detailed model implemented in GEANT 4 [44, 45]. Multiple overlapping pp interactions (pileup) are included in the simulation by overlaying simulated minimum bias events, generated using PYTHIA version 8.160 [46], onto the simulated hard scatter event. The simulated events are weighted such that the distribution of the average number of pp interactions per bunch crossing agrees with data. The simulated events are reconstructed with the same algorithms that are applied to collision data. The underlying event is described with the AUET2 tune [47] for all samples apart from $t\bar{t}$, which uses the Perugia 2011C tune [48], and the Z/γ^*+jets samples which use a SHERPA-specific tune [49].

Stop pair production is modeled using MADGRAPH version 1.5.12 [50] to generate stop-anti-stop pairs using the CTEQ 6L1 parton distribution functions (PDFs) [51], and PYTHIA version 6.427 [52] to perform the R-parity-violating stop decay as well as the parton shower calculation. Stop pairs are generated for

$\Delta R = \sqrt{(\Delta\eta)^2 + (\Delta\phi)^2}$ is used.

stop masses between 400 GeV and 1000 GeV in steps of 100 GeV. Signal cross sections are calculated at next-to-leading order (NLO) in α_s, including the resummation of soft gluon emission at next-to-leading-logarithm accuracy (NLO+NLL) [53–55]. The nominal cross section and the uncertainty are taken from an envelope of cross section predictions using different PDF sets and factorization and renormalization scales, as described in Ref. [56]. The signal samples have cross sections ranging from 356 ± 51 fb for a stop mass of 400 GeV to 0.44 ± 0.12 fb for a stop mass of 1000 GeV. In the simplified models, the stop branching ratios were set to $Br(\tilde{t} \to be) = Br(\tilde{t} \to b\mu) = 0.5$, but the events can be appropriately weighted to give any branching fraction hypothesis. Signal contributions from $\tilde{t} \to b\tau$ decays are not considered.

The largest sources of Standard Model backgrounds are $t\bar{t}$, single top production (Wt channel), and Z/γ^*+jets production. The $t\bar{t}$ process is modeled using the next-to-leading order generator Powheg revision 2129 [57–60] with NLO PDF set CTEQ 6L1 [51], and showered with Pythia version 6.426, When using the baseline Powheg +Pythia $t\bar{t}$ production sample, events are reweighted in bins of the transverse mass (p_{T}) of the $t\bar{t}$ system to match the top quark pair differential cross section observed in ATLAS data [61, 62]. The Wt-channel and s-channel of the single top background are modeled using Powheg revision 1556 [63] with Pythia version 6.426, while the t-channel is modeled using AcerMC version 3.8 [64] with Pythia version 6.426, both with PDF set CTEQ 6L1 [51]. The Z/γ^*+jets production process is modeled using Sherpa version 1.4.1 [49] with NLO PDF set CT10. Charm and bottom quarks are treated as massive.

Other backgrounds considered include di-boson processes, $t\bar{t}$ in association with a vector boson, W boson+jets, and Higgs boson production. These additional background sources are small compared to the three main sources.

4 Event Reconstruction

Events recorded during stable data-taking conditions are analyzed if the reconstructed primary vertex has five or more tracks with $p_{\mathrm{T}} > 400$ MeV associated with it. The primary vertex of an event is identified as the vertex with the highest Σp_T^2 of associated tracks. After the application of beam, detector, and data-quality requirements, the total integrated luminosity considered in this analysis corresponds to 20.3 fb^{-1}. The uncertainty on the integrated luminosity is ±2.8%. It is derived following the same methodology as that detailed in Ref. [65].

Electron candidates are reconstructed from energy deposits in the electromagnetic calorimeter matched to a charged particle track in the ID. Electron candidates must satisfy the *medium++* identification requirement of Ref. [66], have $p_{\mathrm{T}} > 40$ GeV and $|\eta| < 2.47$, and be consistent with the primary vertex with impact parameter significance in the transverse plane $|d_0/\sigma_{d_0}| < 3$ and a longitudinal impact parameter $|z_0 \sin\theta| < 0.4$ mm. Muon candidates are reconstructed by combining tracks in the ID and tracks in the MS [67]. Muon candidates must have $p_{\mathrm{T}} > 40$ GeV and $|\eta| < 2.4$, and be consistent with the primary vertex with $|d_0/\sigma_{d_0}| < 3$ and $|z_0 \sin\theta| < 1.0$ mm. Events containing a poorly measured muon, as determined by having incompatible momentum measurements in the ID and the MS, are rejected. In simulated samples, the efficiencies identifying electrons and muons are corrected to match those found in data.

Jets are reconstructed using the anti-k_t algorithm [68, 69] with a radius parameter $R = 0.4$ from calibrated clusters of energy deposits in the calorimeters. The differences in calorimeter response between electrons, photons and hadrons are taken into account by classifying each cluster, prior to the jet reconstruction, as

coming from an electromagnetic or hadronic shower on the basis of its shape [70]. The jet energy thus accounts for electromagnetic and hadronic energy deposits at the cluster level with correction factors derived from MC simulation. A further correction, used to calibrate the jet energy to the scale of its constituent particles, (JES) [70, 71], is then applied. The impact of pileup is accounted for using a technique, based on jet areas, that provides an event-by-event and jet-by-jet correction [72]. Jets are required to have transverse momentum $p_{\mathrm{T}} > 40$ GeV and $|\eta| < 4.9$. In order to reduce contamination from jets produced by pileup, the scalar sum of the p_{T} of the tracks matched to the jet and originating from the primary vertex must be at least 50% of the scalar sum of the p_{T} of all tracks matched to the jet. This criterion is only applied to jets with $p_{\mathrm{T}} < 50$ GeV and $|\eta| < 2.4$.

Overlaps in the reconstruction of electrons, muons, and jets are removed by the following requirements. If two electrons have $\Delta R < 0.05$, then the lower-p_{T} electron is removed as it is assumed to be from bremsstrahlung followed by pair production. If an electron and a jet have $\Delta R < 0.20$, then the jet is removed as it is assumed to be dominated by the electron. If an electron (muon) and a remaining jet have $\Delta R < 0.40$, then the electron (muon) is removed as it is assumed to be a component of the jet. Of the remaining leptons, if an electron and a muon have $\Delta R < 0.01$, then both are removed. If two muons have $\Delta R < 0.05$, then both are removed. Finally, if two remaining electrons (muons) have an invariant mass less than 12 GeV, then both electrons (muons) are removed to reject leptons from low mass resonances.

After overlap removal, surviving electron (muon) candidates are required to be isolated to suppress heavy flavor decays. The ratio of the sum of the p_{T} of the charged particle tracks within $\Delta R < 0.30$ of the electron (muon) to the minimum of 60 GeV and the p_{T} of the electron (muon) ($\sum_{\Delta R \leq 0.3} p_{\mathrm{T}}^{\mathrm{track}} / \min(p_{\mathrm{T}}, 60\ \mathrm{GeV})$) must be less than 0.1

The identification of b-jets uses the MV1 flavor tagging algorithm [73, 74], which is based on an artificial neural network algorithm that exploits the impact parameters of charged particle tracks, the parameters of reconstructed secondary vertices, and the topology of b- and c-hadron decays inside a jet. The operating point corresponds to an overall 80% b-tagging efficiency, as measured in simulated $t\bar{t}$ events, to a rejection factor of 25 for jets originating from light quarks or gluons, and to a rejection factor of 3 for jets originating from charm quarks. In simulated samples the efficiency of identifying b-jets and the probability of misidentifying jets originating from the fragmentation of light-flavor quarks, gluons, and charm quarks are corrected to match those found in data.

The vector momentum imbalance in the transverse plane is obtained from the negative vector sum of the reconstructed and calibrated physics objects and the calorimeter energy clusters not associated with reconstructed objects. This is denoted as missing transverse momentum, and the symbol $E_{\mathrm{T}}^{\mathrm{miss}}$ is used for its magnitude. The $E_{\mathrm{T}}^{\mathrm{miss}}$ calculation is described elsewhere [75].

5 Event Selection

Events are required to have at least two reconstructed leptons and two b-tagged jets. If more than two leptons or two b-jets are found, the objects with the highest p_{T} are selected. The leptons are required to have opposite charge. Single-electron and single-muon triggers are used to select events. Di-electron and di-muon events are required to pass a single-electron and single-muon trigger respectively, while electron-muon events are selected if either or both of the single-lepton triggers are passed. At least one of the reconstructed leptons is required to be within $\Delta R \leq 0.15$ of the detector signature found by the

trigger. This trigger requirement is highly efficient for signal events; between 93% and 98% of events depending on the flavor channel.

Two overlapping signal regions (SRs) are defined to search for an excess of signal-like events, which are inconsistent with the prediction from the Standard Model alone. In order to achieve a large expected signal to background ratio in the signal regions, MC simulation is used to optimize the selection requirements.

The scalar sum of the p_{T} of the two b-tagged jets and two leptons (H_{T}) effectively separates the signal processes from the major sources of Standard Model background. Events in the SRs are required to have H_{T} above 1100 GeV. Events with two same-flavor leptons with invariant mass within 10 GeV of the Z-boson mass are vetoed to reduce the backgrounds from Z-boson production.

For the signal model, the invariant masses of the two pairs of a lepton and b-tagged jet should be equal since they are decay products of the stop/anti-stop. Therefore, for each of the two possible ways to group two leptons and two b-tagged jets into two pairs of a lepton and a b-tagged jet, the difference in the invariant masses is calculated, $(m^0_{b\ell} - m^1_{b\ell})$, where $m^0_{b\ell}(m^1_{b\ell})$ denotes the mass of the higher (lower)-mass pair. The grouping with the smallest difference is selected. The mass asymmetry is defined as

$$m_{b\ell} \text{ asymmetry} = \frac{m^0_{b\ell} - m^1_{b\ell}}{m^0_{b\ell} + m^1_{b\ell}}. \tag{1}$$

The asymmetry should be close to zero for signal. Standard Model processes, however, have no preference for the mass asymmetry. The SRs require a mass asymmetry of less than or equal to 0.2. Finally, $m^0_{b\ell}$ is used to define the two SRs. SR 400 has a requirement of $m^0_{b\ell} \geq 400$ GeV, and is optimal for lower stop masses, while SR 600 has a requirement of $m^0_{b\ell} \geq 600$ GeV, and is optimal for higher stop masses.

The full selection criteria for the analysis regions is outlined in Table 1 and Figure 2.

Table 1: Summary of signal, control, and validation regions used for this analysis. The control and validation regions are explained in Section 6. All regions require two b-tagged jets and two oppositely charged leptons. An event is in the Z window if it contains two same-flavored leptons with an invariant mass within 10 GeVof the mass of the Z boson.

Region	$m^0_{b\ell}$ [GeV]	H_{T}[GeV]	$E_{\mathrm{T}}^{\mathrm{miss}}$ significance [$\mathrm{GeV}^{1/2}$]	$m_{b\ell}$ asymmetry	Z window
SR 400	≥ 400	≥ 1100	–	≤ 0.2	Veto
SR 600	≥ 600	≥ 1100	–	≤ 0.2	Veto
Top CR	≥ 200	≤ 500	≥ 4	≤ 0.2	Veto
Z CR	≥ 200	≤ 500	≤ 4	≤ 0.2	Select
Top VR 1	≥ 200	≤ 500	< 4	≤ 0.2	Veto
Top VR 2	≥ 200	≤ 500	-	> 0.2	Veto
Top VR 3	≥ 200	> 500	> 4	> 0.2	Veto
Z VR	≥ 200	> 500	–	≤ 0.2	Select

The H_{T}, $m_{b\ell}$ asymmetry, and $m^0_{b\ell}$ distributions are shown in Figure 3 for the simulated background processes and three signal models. In this figure, all the SR selections apart from that on the variable being shown are applied. The number of expected signal events (for the same three signal models) passing each selection requirement is shown in Table 2. The estimates shown in Figure 3 and Table 2 are taken from MC simulation, and the event yields are normalized to 20.3 fb^{-1}.

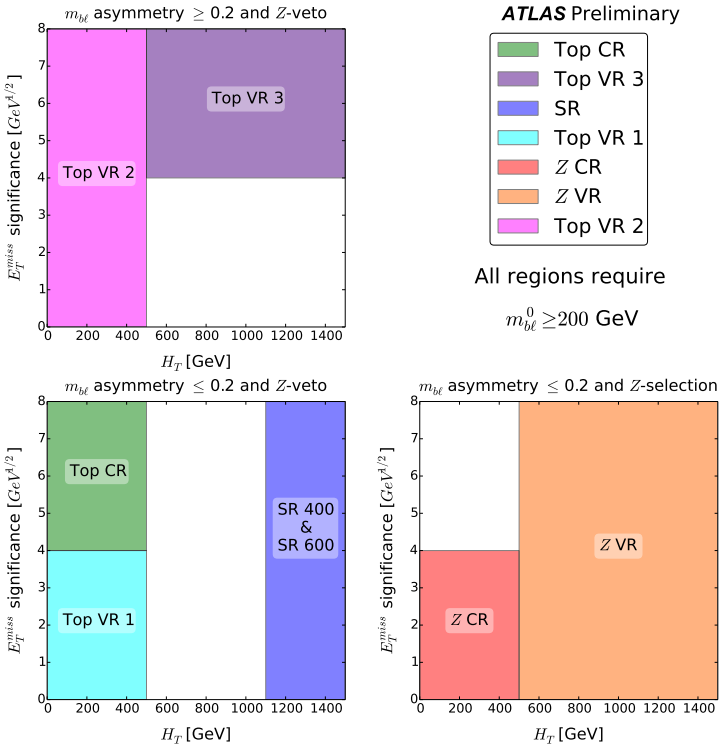

Figure 2: Position of the regions in the $E_{\mathrm{T}}^{\mathrm{miss}}$ significance versus H_{T} space. The two left plots show the $E_{\mathrm{T}}^{\mathrm{miss}}$ significance-H_{T} plane after requiring the invariant mass of the two leptons is not consistent with the Z boson, with the top plot requiring $m_{b\ell}$ asymmetry $\geq$ 0.2 and the bottom requiring $m_{b\ell}$ asymmetry $\leq$ 0.2. The right plot shows the plane when requiring the invariant mass of the two leptons is consistent with the Z boson, and the leptons are of the same flavor. The two SRs apply a different requirement on the invariant mass of the higher-mass $b\ell$ pair. SR 400 requires $m_{b\ell}^0 \geq 400$ GeV, and SR 600 requires $m_{b\ell}^0 \geq 600$ GeV.

6 Background estimation

The background estimates of the $t\bar{t}$ and the Z/γ^*+jets backgrounds use MC simulation normalized in dedicated data control regions (CRs), the top control region (Top CR) and Z control region (Z CR) respectively. The remaining backgrounds are estimated using simulation. Several validation regions (VRs) are defined to validate the extrapolation from the CRs to regions with different kinematics.

Both the Top CR and Z CR require H_{T} to be less than or equal to 500 GeV to reduce the amount of signal contamination in the regions. A cut of $m_{b\ell}$ asymmetry $\leq$ 0.2 is applied to match the signal regions, and $m_{b\ell}^0$ is required to be above 200 GeV. No requirement is made on the invariant mass of the second pair.

The $E_{\mathrm{T}}^{\mathrm{miss}}$ significance variable is used to define CRs that are relatively pure in $t\bar{t}$ or Z/γ^*+jets, where

$$E_{\mathrm{T}}^{\mathrm{miss}} \text{ significance} = \frac{E_{\mathrm{T}}^{\mathrm{miss}}}{\sqrt{H_{\mathrm{T}}}}. \tag{2}$$

Processes like $t\bar{t}$, with real $E_{\mathrm{T}}^{\mathrm{miss}}$, tend to have large $E_{\mathrm{T}}^{\mathrm{miss}}$ significance, while Z/γ^*+jets, where the $E_{\mathrm{T}}^{\mathrm{miss}}$ is from mismeasurement, tend to have low $E_{\mathrm{T}}^{\mathrm{miss}}$ significance. For this reason, the Top CR requires

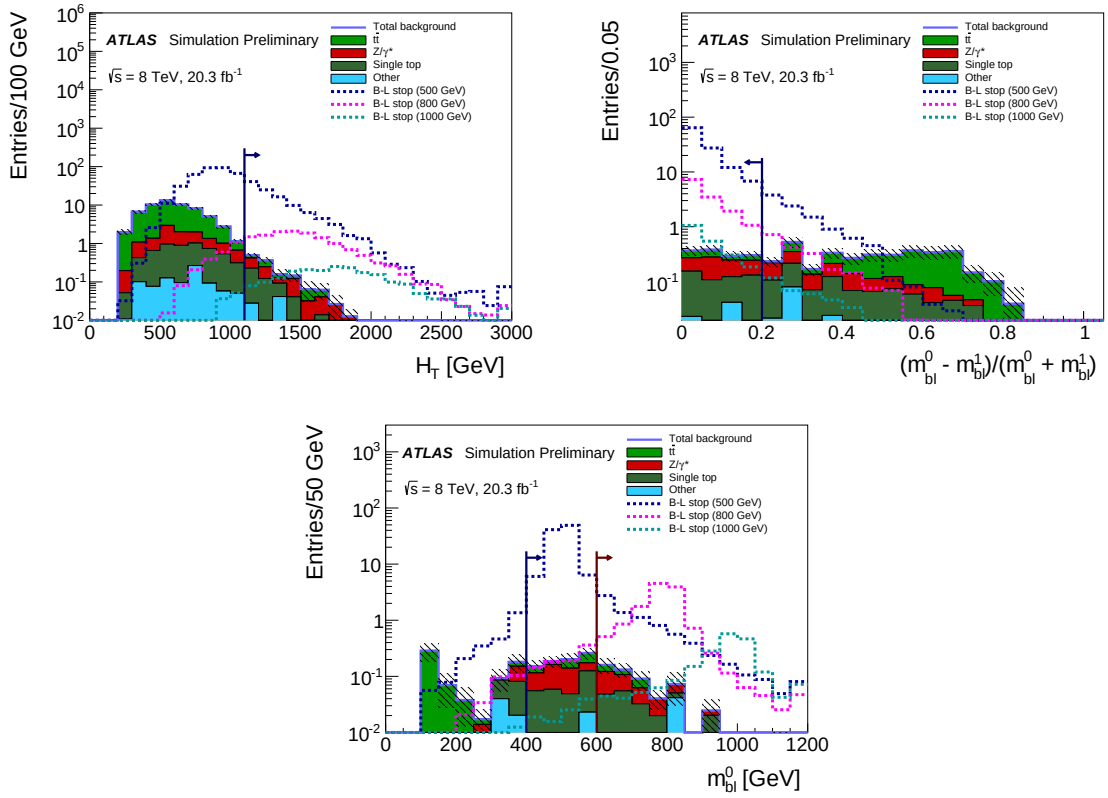

Figure 3: Distributions of the variables which are used to define the SRs. These plots show the MC simulated background samples and three signal models, and are made after applying all the SR selection criteria except for that on the variable shown. The top two plots show the H_{T} and $m_{b\ell}$ asymmetry variables, and the bottom plot shows the $m^0_{b\ell}$ distribution. The arrows show the SR requirement on the variable being shown. In each plot, the last bin includes the overflow for values beyond the maximum shown. The hashed error bands show only the statistical uncertainty on the background MC simulation samples. The signal models have an assumed $Br(\tilde{t} \to be) = Br(\tilde{t} \to b\mu) = 0.5$.

$E_{\mathrm{T}}^{\mathrm{miss}}$ significance ≥ 4 GeV$^{1/2}$ and the Z CR requires $E_{\mathrm{T}}^{\mathrm{miss}}$ significance ≤ 4 GeV$^{1/2}$. The definitions of the CRs, and VRs are summarized in Table 1 and Figure 2.

The normalization of the $t\bar{t}$ and the Z/γ^*+jets backgrounds are determined using a simultaneous fit, which takes into account cross-contamination of the different background processes between the CRs as well as the statistical and systematic uncertainties (described in Section 7) [76]. The remaining background estimates, due to single top and other SM processes, are taken from the MC simulation. The number of observed events as well as the expected number of events in each of the CRs and VRs are shown in Table 3. The agreement between the observed number of events and the fitted event yields in the VRs is summarized in Figure 4. Using the fitted backgrounds, the dominant process in the same-flavor channels of the SRs is Z/γ^*+jets followed by single top and $t\bar{t}$. In the $e\mu$ channel, the Z/γ^*+jets background does not contribute, thus, the largest backgrounds are single top and $t\bar{t}$. As a result of the fit, the Z/γ^*+jets background is scaled up by approximately 40%. Due to this large normalization factor, the background is over-predicted in the Z VR. This over-prediction is taken as an additional systematic uncertainty, described in Section 7.

Table 2: The number of expected signal events pasing each of the signal region cuts. This is shown for stop masses of 500 GeV, 800 GeV, and 1000 GeV. The estimated yields are taken from MC simulation, and are normalized to 20.3 fb^{-1}, and the uncertainty given is the MC statistical uncertainty. The signal models have an assumed branching fraction of $Br(\tilde{t} \to be) = Br(\tilde{t} \to b\mu) = 0.5$.

Selection	$m_{\tilde{t}}$ = 500 GeV	$m_{\tilde{t}}$ = 800 GeV	$m_{\tilde{t}}$ = 1000 GeV
$\sigma \cdot L$	1750 ± 260	59 ± 12	8.9 ± 2.5
$bb\ell\ell$	624 ± 4	19.65 ± 0.18	2.68 ± 0.05
Z veto	619 ± 4	19.62 ± 0.18	2.68 ± 0.05
$H_T \geq 1100$ GeV	122.9 ± 1.8	16.01 ± 0.17	2.50 ± 0.04
$m_{b\ell}$ asymmetry ≤ 0.2	112.8 ± 1.7	14.00 ± 0.15	2.11 ± 0.04
$m_{b\ell} \geq 400$ GeV	110.3 ± 1.7	13.74 ± 0.15	2.09 ± 0.04
$m_{b\ell} \geq 600$ GeV	7.7 ± 0.4	12.86 ± 0.15	1.99 ± 0.04

Table 3: The observed and expected event yields in the CRs and VRs. The expected event yields are shown before and after a fit to the data in the CRs. The fitted background yields in the CRs match the observed number of events in data by construction.

	Top CR	Z CR	Top VR 1	Top VR 2	Top VR 3	Z VR
Observed	369	327	645	606	67	101
Fitted background	369 ± 19	327 ± 18	690 ± 50	630 ± 40	72 ± 5	130 ± 60
Fitted $t\bar{t}$	346 ± 19	9.1 ± 0.7	600 ± 40	497 ± 35	54 ± 5	2.99 ± 0.24
Fitted Z/γ^*+jets	3.2 ± 0.5	309 ± 18	63 ± 5	64 ± 5	1.5 ± 0.8	120 ± 60
Single top	16.7 ± 2.0	0.83 ± 0.09	23.0 ± 2.6	56 ± 6	14.1 ± 1.9	0.32 ± 0.04
Other	2.83 ± 0.27	8.64 ± 1.0	4.7 ± 0.4	8.2 ± 0.8	2.03 ± 0.27	6.4 ± 0.7
Input SM	330	230	614	557	66	93
Input $t\bar{t}$	310	8.2	543	447	49	2.7
Input Z/γ^*+jets	2.2	220	44	45	1.1	83
Input single top	17	0.8	23	57	14	0.30
Input other	2.8	8.6	4.7	8.2	2.0	6.40

The extrapolation from low H_{T} CRs to the high H_{T} region where the SRs are located is validated using the Top VR 3 and Z VR. These validation regions show fair agreement between the observed and predicted event yields as well as for the shape of the $m^0_{b\ell}$ and H_{T} distributions as shown in Figures 5 and 6.

7 Systematic uncertainties

Several sources of systematic uncertainty are considered when determining the estimated signal and background contributions. The largest sources of systematic uncertainty are those related to the MC statistical

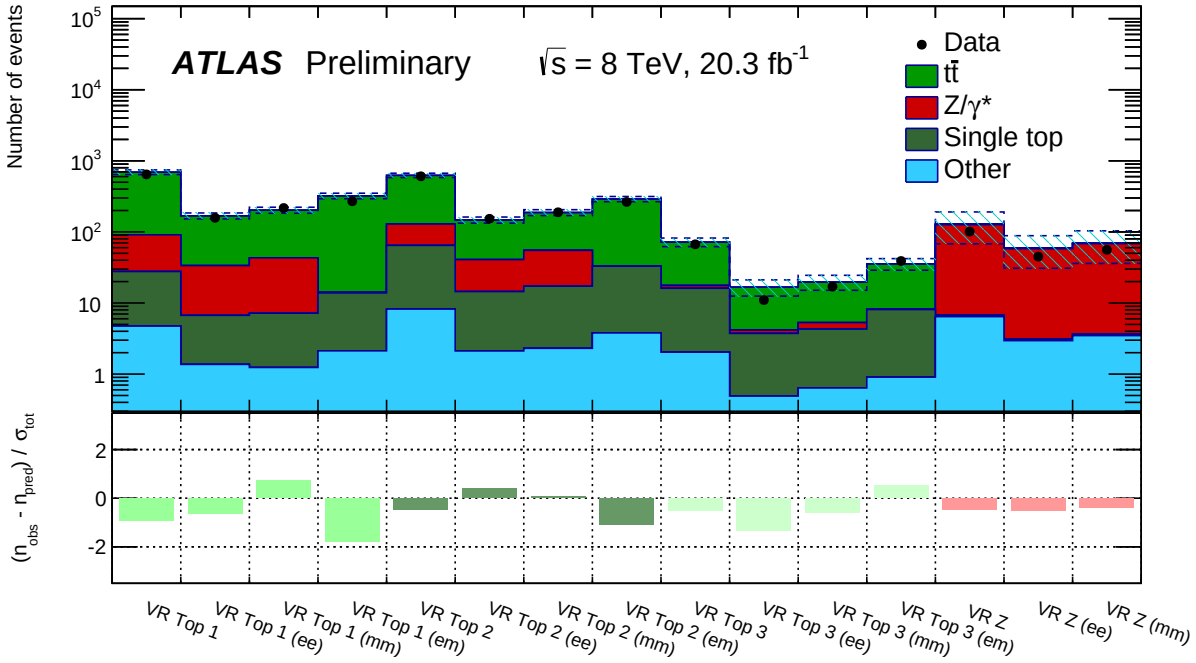

Figure 4: The top of this plot shows the number of observed and expected events in the validation regions, and broken down by flavor channel. The uncertainty band includes the statistical uncertainty as well as the systematic uncertainty (described in Section 7). The bottom of the plot shows the deviation of that channel's prediction from the observed number of events divided by the uncertainty on the prediction. The normalization of the background yields are determined by fitting the $t\bar{t}$ and Z/γ^*+jets backgrounds to the observed data in the two CRs.

uncertainty in the SRs, the JES, the b-tagging efficiency and the extrapolation of the Z/γ^*+jets background to high H_{T}. The uncertainty on the lepton energy scale and resolution was considered, but shown to be negligible.

- **Jet energy scale**: The uncertainty on the JES takes into account the dependence on p_{T}, η, jet flavor, and the number of primary vertices. The components of the JES uncertainty are varied by $\pm 1\sigma$ in the MC simulation and propagated to the expected event yield.
- ***b*-tagging**: The uncertainty on the b-tagging efficiency is evaluated by varying the correction factors applied to each jet in the simulation within a range that reflects the systematic uncertainty on the measured tagging and rejection efficiencies. These uncertainties take into account the dependence on p_{T} and jet flavor.
- **Jet energy resolution**: The uncertainty on the jet energy resolution (JER) is evaluated by applying an additional smearing to the p_{T} of each of the jets in the simulation. This smearing is then propagated to the expected event yield.
- **H_{T} extrapolation**: An H_{T} extrapolation uncertainty of 50% is applied to Z/γ^*+jets events with $H_{\mathrm{T}} \geq 500$ GeV. This is assigned to account for uncertainty on the Z/γ^*+jets H_{T} spectrum. This uncertainty is derived from the disagreement observed in Figures 4-6.

Several theoretical uncertainties are considered in the modeling of the major background processes in MC simulation. These include the uncertainty on the single top (Wt) cross section, the uncertainty related to

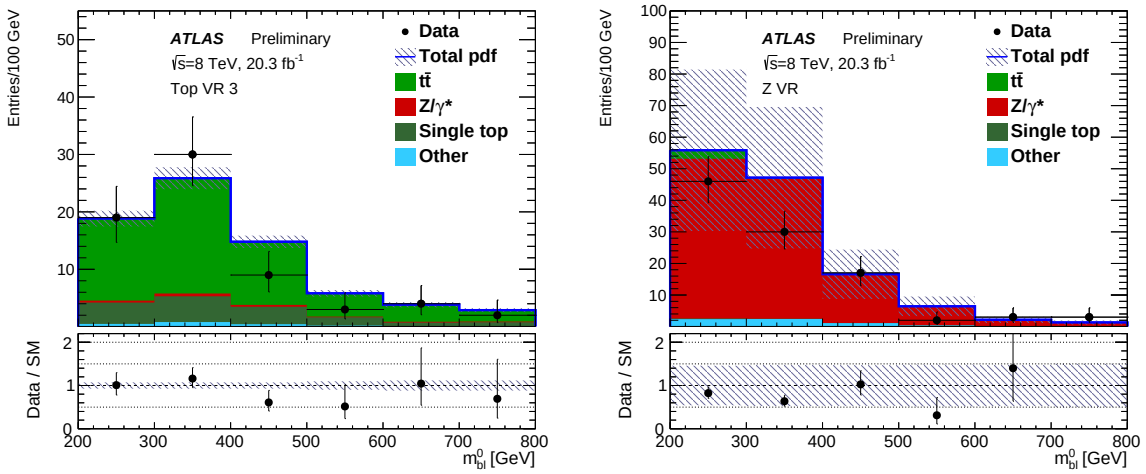

Figure 5: The $m^0_{b\ell}$ distribution in Top VR 3 (left) and Z VR (right). The Standard Model background prediction is shown after setting the normalization of the $t\bar{t}$ and Z/γ^*+jets backgrounds based on the observed data in the CRs. The hashed bands show the uncertainty on the fitted background prediction including all statistical and systematics uncertainties. The bottom of each plot shows the ratio of the observed data to the Standard Model background prediction.

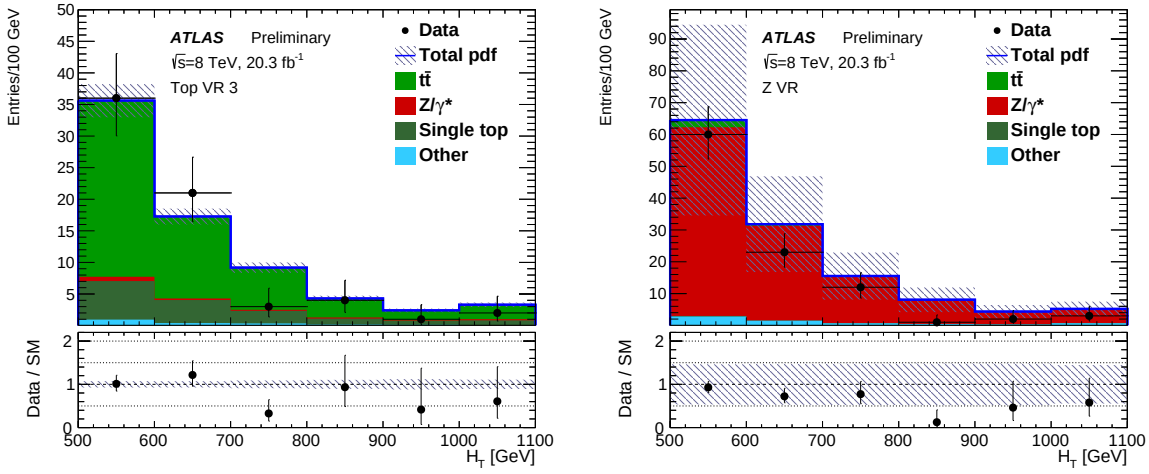

Figure 6: The H_{T} distribution in Top VR 3 (left) and Z VR (right). The Standard Model background prediction is shown after setting the normalization of the $t\bar{t}$ and Z/γ^*+jets backgrounds based on the observed data in the CRs. The hashed bands show the uncertainty on the fitted background prediction including all statistical and systematics uncertainties. The bottom of each plot shows the ratio of the observed data to the Standard Model background prediction.

the renormalization and factorization scales, parton shower, and the limited number of partons included in the matrix element calculation. These theoretical uncertainties are on the order of a few percent of the total background prediction. The uncertainty on the luminosity is assessed for the signal processes, and all background processes apart from $t\bar{t}$ and Z/γ^*+jets, whose normalizations are determined using data. The relative systematic uncertainty on the total background estimate in the SRs is shown in Table 4

Table 4: Summary of the effect of each considered sources of systematic uncertainty on the background estimate in SR 400 and SR 600. Several sources of theoretical systematic uncertainty which have a small effect on the total background estimate are grouped into the "Other theory" category.

Systematic Uncertainty (%)	SR 400	SR 600
JES	15	3
b-tagging	13	12
JER	5	1
Luminosity	1	1
H_{T} extrapolation	19	20
MC statistical	13	23
CR statistical	3	3
Wt cross section	2	2
Other theory	1	2

For each of the signal models, the effects of uncertainty on the JES, b-tagging efficiency, JER, and luminosity are considered as well as the uncertainty on the signal model cross section which ranges between 14% and 28%.

8 Results

The background yields in these signal regions are determined by a maximum likelihood fit [76] for the $t\bar{t}$ and Z/γ^*+jets normalizations, which are constrained by the observed data in the Top and Z control regions. The systematic uncertainties described previously are included as Gaussian-distributed nuisance parameters. The fitted background yields and the observed number of events in each signal region are shown in Tables 5 and 6. Two events are observed, in agreement with the Standard Model prediction. The kinematics of the two selected events are shown in Table 7, the $m^0_{b\ell}$ and H_{T} distributions in SR 400 are shown in Figure 7.

As the observed number of events is consistent with the Standard Model prediction, Upper limits at 95% confidence level (CL) on the number of beyond the Standard Model (BSM) events for each signal region are derived using the CL_s prescription and neglecting any possible contamination in the control regions. Normalizing these by the integrated luminosity of the data sample they can be interpreted as upper limits on the visible BSM cross section, σ_{vis}, where σ_{vis} is defined as the product of acceptance, reconstruction efficiency and production cross section. The results are given in Tables 5 and 6.

Exclusion limits on the signal model are determined using the CL_S prescription based on a simultaneous fit of the SRs and CRs [76]. The predicted signal contamination is taken into account in the CRs. For each stop mass, exclusion fits are performed with various assumptions on the branching ratios of the stop. For

Table 5: The expected and observed event yields in SR 400. The expected event yields are shown before and after performing the fit to the data in the control regions. The last three rows show the model-independent 95% CL on the visible cross section and the number of events (expected and observed) in SR 400 from a generic non-Standard Model process.

	SR 400	SR 400 ee	SR 400 $\mu\mu$	SR 400 $e\mu$
Observed	2	0	2	0
Fitted background	1.39 ± 0.35	0.36 ± 0.15	0.57 ± 0.20	0.45 ± 0.11
Fitted $t\bar{t}$	0.33 ± 0.09	0.07 ± 0.08	0.07 ± 0.02	0.19 ± 0.05
Fitted Z/γ^*+jets	0.54 ± 0.28	0.20 ± 0.10	0.35 ± 0.18	≤ 0.01
Single Top	0.44 ± 0.08	0.10 ± 0.03	0.11 ± 0.03	0.23 ± 0.05
Other	0.07 ± 0.04	≤ 0.01	0.04 ± 0.02	0.03 ± 0.03
Input SM	1.2	0.30	0.46	0.43
Input $t\bar{t}$	0.30	0.06	0.06	0.17
Input Z/γ^*+jets	0.38	0.14	0.24	0.00
Input single Top	0.44	0.10	0.11	0.23
Input other	0.07	0.00	0.04	0.03
σ_{vis} [fb]	0.23	0.11	0.26	0.11
Observed $N_{\text{non-SM}}$	4.8	2.2	5.4	2.3
Expected $N_{\text{non-SM}}$	$4.0^{+2.2}_{-1.1}$	$3.2^{+1.7}_{-1.1}$	$3.6^{+1.9}_{-1.5}$	$3.3^{+1.8}_{-1.3}$

each point on the branching ratio plane, the SR which provided the best expected sensitivity, as measured by the lowest expected CL_S value, is chosen. The expected and observed limits are shown in Figure 8. This figure shows, for each simulated stop mass, the observed (expected) 95% exclusion limit on the branching fraction under the red (blue) line. A yellow band shows the $\pm 1\sigma$ uncertainty on the expected limit, determined from the systematic uncertainty on the signal and background prediction excluding the effect of the signal cross section uncertainty. The effect of varying the signal cross section on the observed limit is indicated by the dashed red lines. The final limit on the stop mass is shown in Figure 9. This plot shows the 95% confidence limit (CL) on the mass obtained by choosing the maximum excluded mass for each branching ratio on the plane using the nominal cross section value. As the branching ratio of $\tilde{t} \rightarrow b\tau$ increases, the number of expected events with electrons or muons in the final state decreases for the same simulated stop mass. Therefore, the limit on the mass is strongest at the bottom of the plane. In the top corner of the plot, the SRs described in this analysis note have no sensitivity, however traditional lepto-quark searches for final states with b-tagged jets and τ leptons are able to place experimental limits in this region [35].

Table 6: The expected and observed event yields in SR 600. The expected event yields are shown before and after performing the fit to the data in the control regions. The last three rows show the model-independent 95% CL on the visible cross section and the number of events (expected and observed) in SR 600 from a generic non-Standard Model process.

	SR 600	SR 600 ee	SR 600 $\mu\mu$	SR 600 $e\mu$
Observed	1	0	1	0
Fitted background	0.55 ± 0.15	0.15 ± 0.06	0.24 ± 0.10	0.16 ± 0.06
Fitted $t\bar{t}$	0.10 ± 0.02	0.03 ± 0.01	≤ 0.01	0.07 ± 0.03
Fitted Z/γ^*+jets	0.23 ± 0.12	0.08 ± 0.05	0.15 ± 0.08	≤ 0.01
Single Top	0.18 ± 0.04	0.03 ± 0.01	0.05 ± 0.02	0.09 ± 0.03
Other	0.04 ± 0.01	≤ 0.01	0.04 ± 0.02	≤ 0.01
Input SM	0.47	0.12	0.20	0.16
Input $t\bar{t}$	0.09	0.03	0.00	0.06
Input Z/γ^*+jets	0.16	0.06	0.10	0.00
Input single Top	0.18	0.03	0.05	0.09
Input other	0.04	0.00	0.04	0.00
σ_{vis} [fb]	0.19	0.10	0.20	0.10
Observed $N_{\text{non-SM}}$	3.9	2.1	4.0	2.1
Expected $N_{\text{non-SM}}$	$3.5^{+1.9}_{-1.4}$	$2.6^{+1.6}_{-0.6}$	$3.0^{+1.7}_{-1.0}$	$2.7^{+1.6}_{-0.7}$

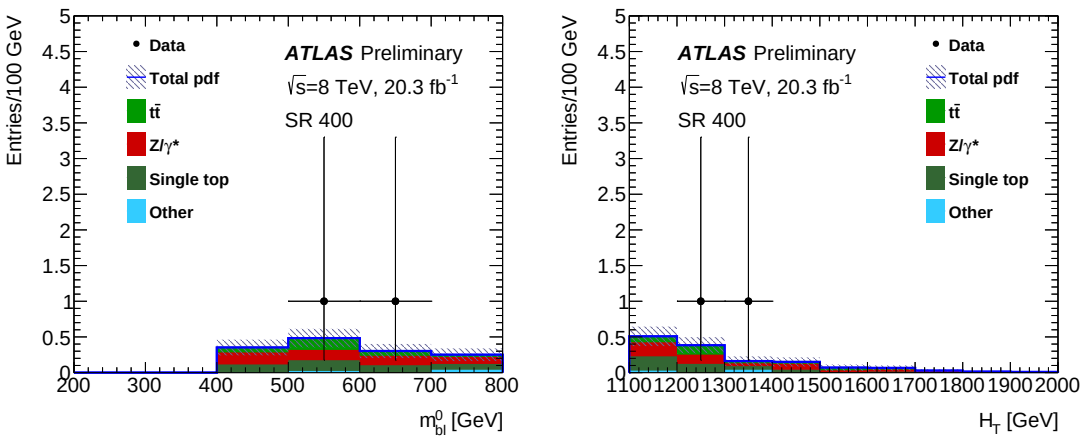

Figure 7: These plots show the $m^0_{b\ell}$ (left) and H_{T} (right) distributions in SR 400. The Standard Model background prediction is taken from the fitted background prediction. The hashed bands show the uncertainty on the fitted background prediction including the MC statistical and sources of systematic uncertainty. The bottom of each plot shows the ratio of the observed data to the Standard Model background prediction.

Table 7: The event and object kinematics for the two events passing the signal region selection. The first event passes the SR 400 selection while the second event passes both SR 400 and SR 600 selections.

Run number	214216	210302
Event number	121272046	2292645861
$m^0_{b\ell}$ [GeV]	558	686
ℓ_0 flavor	μ	μ
ℓ_0 charge	−	−
ℓ_0 p_{T} [GeV]	375	272
b_0 p_{T} [GeV]	330	460
ℓ_0 η	−0.11	1.22
b_0 η	0.56	0.95
ℓ_0 ϕ	2.0	−1.3
b_0 ϕ	−2.7	2.5
$m^1_{b\ell}$ [GeV]	526	528
ℓ_1 flavor	μ	μ
ℓ_1 charge	+	+
ℓ_1 p_{T} [GeV]	88	96
b_1 p_{T} [GeV]	542	374
ℓ_1 η	0.45	1.43
b_1 η	−1.1	−0.26
ℓ_1 ϕ	−2.3	−0.91
b_1 ϕ	−0.21	2.3
$m_{b\ell}$ asymmetry	0.03	0.13
H_{T} [GeV]	1335	1203
$E_{\mathrm{T}}^{\mathrm{miss}}$ significance [$\mathrm{GeV}^{1/2}$]	2.9	6.4
$E_{\mathrm{T}}^{\mathrm{miss}}$ [GeV]	107	223
$m_{\ell\ell}$ [GeV]	324	71

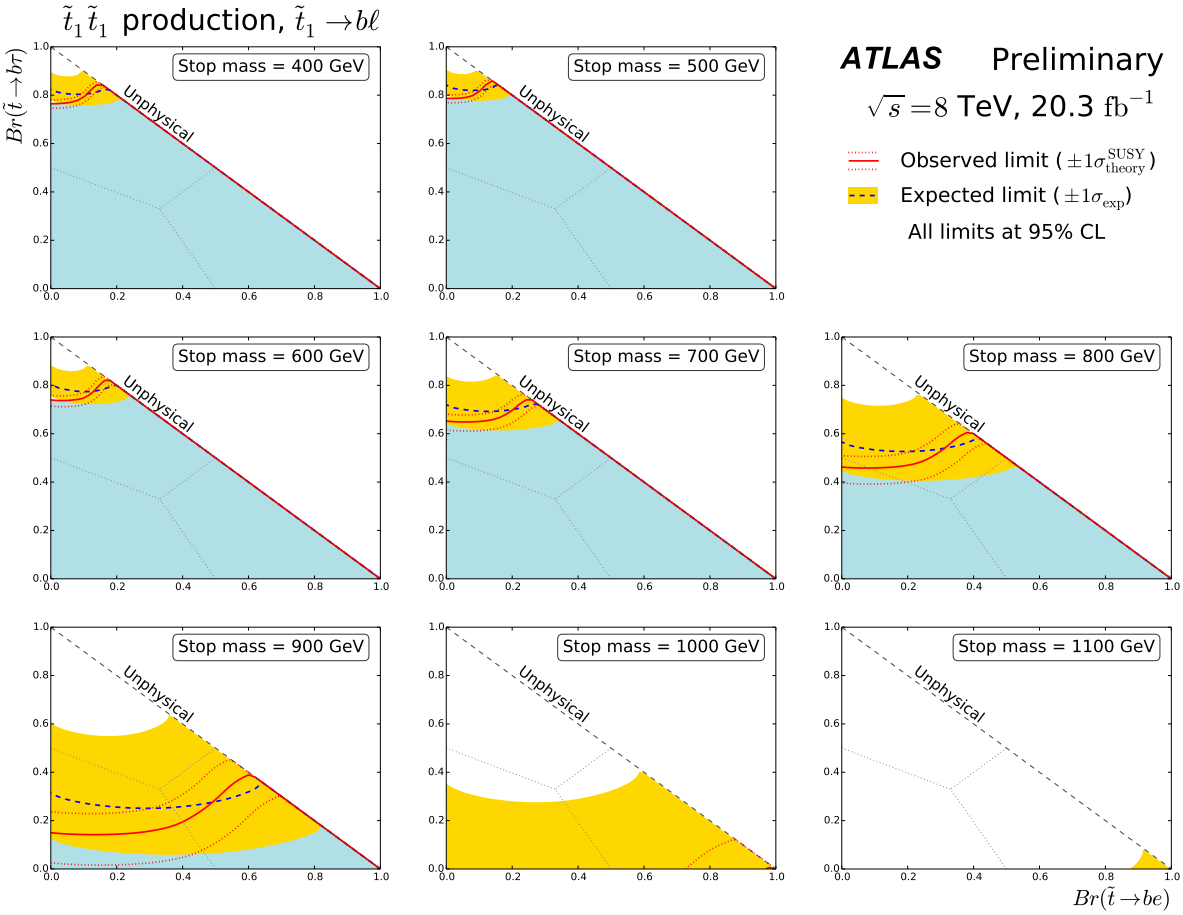

Figure 8: Expected and observed limit on the branching ratios for the stop decaying to different lepton flavors shown for different stop mass hypotheses between 400 GeV and 1 TeV. The shaded area under the solid line represents the branching ratios which are excluded at 95% CL for each stop mass. The dotted lines represent the uncertainty on the observed mass limit obtained by varying the signal model cross section up and down one standard deviation from the nominal value. The dashed line shows the expected 95% CL exclusion for each stop mass, and the shaded band shows the uncertainty on this expected exclusion limit from statistical uncertainty and the sources of systematic uncertainty discussed in Section 7.

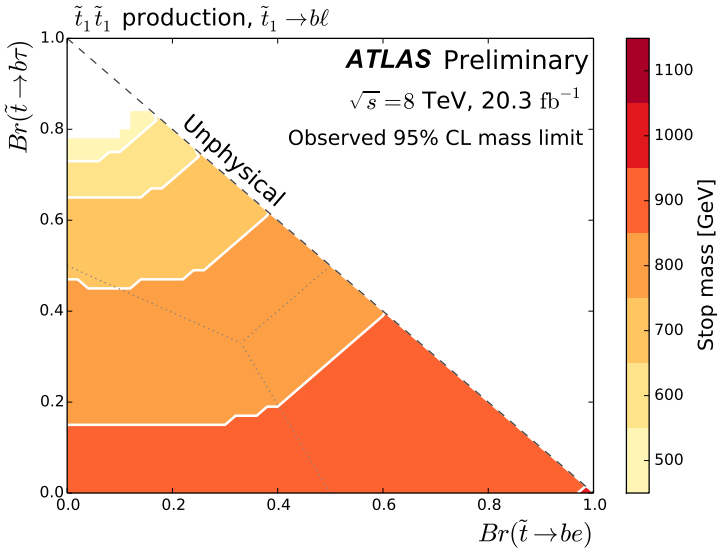

Figure 9: The observed mass limit on the stop at 95% CL. This limit is obtained using the nominal stop cross section. Stop masses between 400 GeV and 1100 GeV, in steps of 100 GeV, were tested. The mass limit shown corresponds to the highest-mass stop sample which was excluded. As the branching ratio of $\tilde{t} \to b\tau$ increases, the number of expected events with electrons or muons in the final state decreases. Therefore, the limit on the mass decreases.

9 Conclusion

A search for direct stop pair production, where the stop particles each decay via an R-parity-violating coupling to a b-quark and an electron or muon, leading to final states with two b-tagged jets and two light leptons (electron or muon). The search uses 20.3 fb^{-1}of $\sqrt{s}$ = 8 TeV proton-proton data collected with the ATLAS detector at the LHC. No significant excess of events over the Standard Model prediction is observed, and limits are set on the mass of the stop at 95% confidence level. A scan of possible stop branching ratios are tested, the mass limit ranges between 500 GeV, when the stop has a branching ratio to a b-quark and a tau lepton of 80%, to to 1 TeVwhen the stop decays entirely to a b-quark and an electron.

Acknowledgements

We thank CERN for the very successful operation of the LHC, as well as the support staff from our institutions without whom ATLAS could not be operated efficiently.

We acknowledge the support of ANPCyT, Argentina; YerPhI, Armenia; ARC, Australia; BMWFW and FWF, Austria; ANAS, Azerbaijan; SSTC, Belarus; CNPq and FAPESP, Brazil; NSERC, NRC and CFI, Canada; CERN; CONICYT, Chile; CAS, MOST and NSFC, China; COLCIENCIAS, Colombia; MSMT CR, MPO CR and VSC CR, Czech Republic; DNRF, DNSRC and Lundbeck Foundation, Denmark; EPLANET, ERC and NSRF, European Union; IN2P3-CNRS, CEA-DSM/IRFU, France; GNSF, Georgia; BMBF, DFG, HGF, MPG and AvH Foundation, Germany; GSRT and NSRF, Greece; RGC, Hong Kong SAR, China; ISF, MINERVA, GIF, I-CORE and Benoziyo Center, Israel; INFN, Italy; MEXT and JSPS, Japan; CNRST, Morocco; FOM and NWO, Netherlands; BRF and RCN, Norway; MNiSW and NCN, Poland; GRICES and FCT, Portugal; MNE/IFA, Romania; MES of Russia and ROSATOM, Russian Federation; JINR; MSTD, Serbia; MSSR, Slovakia; ARRS and MIZŠ, Slovenia; DST/NRF, South Africa; MINECO, Spain; SRC and Wallenberg Foundation, Sweden; SER, SNSF and Cantons of Bern and Geneva, Switzerland; NSC, Taiwan; TAEK, Turkey; STFC, the Royal Society and Leverhulme Trust, United Kingdom; DOE and NSF, United States of America.

The crucial computing support from all WLCG partners is acknowledged gratefully, in particular from CERN and the ATLAS Tier-1 facilities at TRIUMF (Canada), NDGF (Denmark, Norway, Sweden), CC-IN2P3 (France), KIT/GridKA (Germany), INFN-CNAF (Italy), NL-T1 (Netherlands), PIC (Spain), ASGC (Taiwan), RAL (UK) and BNL (USA) and in the Tier-2 facilities worldwide.

References

[1] H. Miyazawa, *Baryon Number Changing Currents*, Prog. Theor. Phys. **36 (6)** (1966) 1266–1276.

[2] P. Ramond, *Dual Theory for Free Fermions*, Phys. Rev. **D3** (1971) 2415–2418.

[3] Y. A. Golfand and E. P. Likhtman,
Extension of the Algebra of Poincare Group Generators and Violation of p Invariance,
JETP Lett. **13** (1971) 323–326.

[4] A. Neveu and J. H. Schwarz, *Factorizable Dual Model of Pions*, Nucl. Phys. **B31** (1971) 86–112.

[5] A. Neveu and J. H. Schwarz, *Quark Model of Dual Pions*, Phys. Rev. **D4** (1971) 1109–1111.

[6] J. Gervais and B. Sakita, *Field Theory Interpretation of Supergauges in Dual Models*,
Nucl. Phys. **B34** (1971) 632–639.

[7] D. V. Volkov and V. P. Akulov, *Is the Neutrino a Goldstone Particle?*
Phys. Lett. **B46** (1973) 109–110.

[8] J. Wess and B. Zumino, *A Lagrangian Model Invariant Under Supergauge Transformations*,
Phys. Lett. **B49** (1974) 52.

[9] J. Wess and B. Zumino, *Supergauge Transformations in Four-Dimensions*,
Nucl. Phys. **B70** (1974) 39–50.

[10] P. Fayet, *Supersymmetry and Weak, Electromagnetic and Strong Interactions*,
Phys. Lett. **B64** (1976) 159.

[11] P. Fayet, *Spontaneously Broken Supersymmetric Theories of Weak, Electromagnetic and Strong Interactions*, Phys. Lett. **B69** (1977) 489.

[12] G. R. Farrar and P. Fayet, *Phenomenology of the Production, Decay, and Detection of New Hadronic States Associated with Supersymmetry*, Phys. Lett. **B76** (1978) 575–579.

[13] P. Fayet, *Relations Between the Masses of the Superpartners of Leptons and Quarks, the Goldstino Couplings and the Neutral Currents*, Phys. Lett. **B84** (1979) 416.

[14] S. Dimopoulos and H. Georgi, *Softly Broken Supersymmetry and SU(5)*,
Nucl. Phys. **B193** (1981) 150.

[15] P. Fileviez Perez and S. Spinner, *Spontaneous R-Parity Breaking and Left-Right Symmetry*,
Phys. Lett. **B673** (2009) 251–254, arXiv: 0811.3424 [hep-ph].

[16] V. Barger, P. Fileviez Perez, and S. Spinner,
Minimal Gauged $U(1)_{B-L}$ Model with Spontaneous R-Parity Violation,
Phys. Rev. Lett. **102** (2009) 181802, arXiv: 0812.3661 [hep-ph].

[17] P. Fileviez Perez and S. Spinner, *Spontaneous R-Parity Breaking in SUSY Models*,
Phys. Rev. **D80** (2009) 015004, arXiv: 0904.2213 [hep-ph].

[18] L. L. Everett, P. Fileviez Perez, and S. Spinner,
The Right Side of TeV Scale Spontaneous R-Parity Violation, Phys. Rev. **D80** (2009) 055007,
arXiv: 0906.4095 [hep-ph].

[19] M. Evans and B. A. Ovrut, *The World Sheet Supergravity of the Heterotic String*,
Phys. Lett. **B171** (1986) 177.

[20] A. Lukas et al., *The Universe As a Domain Wall*, Phys. Rev. **D59** (1999) 086001,
arXiv: hep-th/9803235 [hep-th].

[21] V. Braun et al., *A Heterotic Standard Model*, Phys. Lett. **B618** (2005) 252–258, arXiv: hep-th/0501070 [hep-th].

[22] V. Braun et al., *The Exact MSSM Spectrum From String Theory*, J. High Energy Phys. **0605** (2006) 043, arXiv: hep-th/0512177 [hep-th].

[23] V. Braun, Y.-H. He, and B. A. Ovrut, *Stability of the Minimal Heterotic Standard Model Bundle*, J. High Energy Phys. **0606** (2006) 032, arXiv: hep-th/0602073 [hep-th].

[24] M. Ambroso and B. Ovrut, *The B-L/Electroweak Hierarchy in Heterotic String and M-Theory*, J. High Energy Phys. **0910** (2009) 011, arXiv: 0904.4509 [hep-th].

[25] M. Ambroso and B. A. Ovrut, *The Mass Spectra, Hierarchy and Cosmology of B-L MSSM Heterotic Compactifications*, Int. J. Mod. Phys. **A26** (2011) 1569–1627, arXiv: 1005.5392 [hep-th].

[26] B. A. Ovrut, A. Purves, and S. Spinner, *Wilson Lines and a Canonical Basis of SU(4) Heterotic Standard Models*, J. High Energy Phys. **1211** (2012) 026, arXiv: 1203.1325 [hep-th].

[27] P. Fileviez Perez and S. Spinner, *The Minimal Theory for R-parity Violation at the LHC*, J. High Energy Phys. **1204** (2012) 118, arXiv: 1201.5923 [hep-ph].

[28] P. Fileviez Perez and S. Spinner, *Supersymmetry at the LHC and the Theory of R-parity*, Phys. Lett. **B728** (2014) 489–495, arXiv: 1308.0524 [hep-ph].

[29] B. A. Ovrut, A. Purves, and S. Spinner, *A Statistical Analysis of the Minimal SUSY B-L Theory* (2014), arXiv: 1412.6103 [hep-ph].

[30] B. A. Ovrut, A. Purves, and S. Spinner, *The Minimal SUSY $B - L$ Model: From the Unification Scale to the LHC* (2015), arXiv: 1503.01473 [hep-ph].

[31] R. Barbieri and G. Giudice, *Upper Bounds on Supersymmetric Particle Masses*, Nucl. Phys. **B306** (1988) 63.

[32] B. de Carlos and J. Casas, *One Loop Analysis of the Electroweak Breaking in Supersymmetric Models and the Fine Tuning Problem*, Phys. Lett. **B309** (1993) 320–328, arXiv: hep-ph/9303291 [hep-ph].

[33] Z. Marshall et al., *LSP Squark Decays at the LHC and the Neutrino Mass Hierarchy*, Phys. Rev. **D90**.1 (2014) 015034, arXiv: 1402.5434 [hep-ph].

[34] Z. Marshall et al., *Spontaneous R-Parity Breaking, Stop LSP Decays and the Neutrino Mass Hierarchy*, Phys. Lett. **B732** (2014) 325–329, arXiv: 1401.7989 [hep-ph].

[35] ATLAS Collaboration, *Search for Third Generation Scalar Leptoquarks in pp Collisions at $\sqrt{s} = 7$ TeV with the ATLAS Detector*, J. High Energy Phys. **1306** (2013) 033, arXiv: 1303.0526 [hep-ex].

[36] ATLAS Collaboration, *Search for Second Generation Scalar Leptoquarks in pp Collisions at $\sqrt{s} = 7$ TeV with the ATLAS Detector*, Eur. Phys. J. **C72** (2012) 2151, arXiv: 1203.3172 [hep-ex].

[37] ATLAS Collaboration, *Search for First Generation Scalar Leptoquarks in pp Collisions at $\sqrt{s} = 7$ TeV with the ATLAS Detector*, Phys. Lett. **B709** (2012) 158–176, arXiv: 1112.4828 [hep-ex].

[38] ATLAS Collaboration, *Search for Pair Production of First or Second Generation Leptoquarks in Proton-Proton Collisions at $\sqrt{s}$ = 7 TeV Using the ATLAS Detector at the LHC*, Phys. Rev. **D83** (2011) 112006, arXiv: 1104.4481 [hep-ex].

[39] CMS Collaboration, *Search for Pair Production of Third-Generation Scalar Leptoquarks and Top Squarks in Proton-Proton Collisions at $\sqrt{s}$ = 8 TeV*, Phys. Lett. **B739** (2014) 229, arXiv: 1408.0806 [hep-ex].

[40] CMS Collaboration, *Search for Pair-production of First Generation Scalar Leptoquarks in pp Collisions at $\sqrt{s}$ = 8 TeV*, Report No. CMS-PAS-EXO-12-041 (2014), URL: https://cds.cern.ch/record/1742179.

[41] CMS Collaboration, *Search for Pair Production of Third-Generation Leptoquarks and Top Squarks in pp Collisions at $\sqrt{s}$ = 7 TeV*, Phys. Rev. Lett. **110**.8 (2013) 081801, arXiv: 1210.5629 [hep-ex].

[42] CMS Collaboration, *Search for Pair Production of First- and Second-Generation Scalar Leptoquarks in pp Collisions at $\sqrt{s}$ = 7 TeV*, Phys. Rev. **D86** (2012) 052013, arXiv: 1207.5406 [hep-ex].

[43] ATLAS Collaboration, *The ATLAS Experiment at the CERN Large Hadron Collider*, JINST **3** (2008).

[44] S. Agostinelli et al., *GEANT4: A Simulation Toolkit*, Nucl. Instrum. Meth. **A506** (2003) 250–303.

[45] ATLAS Collaboration, *The ATLAS Simulation Infrastructure*, European Physical Journal C **70** (2010) 823–874, arXiv: 1005.4568 [physics.ins-det].

[46] T. Sjöstrand, S. Mrenna, and P. Z. Skands, *A Brief Introduction to PYTHIA 8.1*, Comput.Phys.Commun. **178** (2008) 852–867, arXiv: 0710.3820 [hep-ph].

[47] ATLAS Collaboration, *New ATLAS Event Generator Tunes to 2010 Data*, Report No. ATL-PHYS-PUB-2011-008 (2011), URL: https://cds.cern.ch/record/1345343.

[48] P. Z. Skands, *Tuning Monte Carlo Generators: The Perugia Tunes*, Phys. Rev. **D82** (2010) 074018, arXiv: 1005.3457 [hep-ph].

[49] T. Gleisberg et al., *Event Generation with SHERPA 1.1*, J. High Energy Phys. **0902** (2009) 007, arXiv: 0811.4622 [hep-ph].

[50] J. Alwall et al., *MadGraph 5 : Going Beyond*, J. High Energy Phys. **1106** (2011) 128, arXiv: 1106.0522 [hep-ph].

[51] P. M. Nadolsky et al., *Implications of CTEQ Global Analysis for Collider Observables*, Phys. Rev. **D78** (2008) 013004, arXiv: 0802.0007 [hep-ph].

[52] T. Sjöstrand., S. Mrenna, and P. Z. Skands, *PYTHIA 6.4 Physics and Manual*, J. High Energy Phys. **0605** (2006) 026, arXiv: hep-ph/0603175 [hep-ph].

[53] W. Beenakker et al., *Stop Production at Hadron Colliders*, Nucl. Phys. **B515** (1998) 3–14, arXiv: hep-ph/9710451 [hep-ph].

[54] W. Beenakker et al., *Supersymmetric Top and Bottom Squark Production at Hadron Colliders*, J. High Energy Phys. **1008** (2010) 098, arXiv: 1006.4771 [hep-ph].

[55] W. Beenakker et al., *Squark and Gluino Hadroproduction*, Int. J. Mod. Phys. **A26** (2011) 2637–2664, arXiv: 1105.1110 [hep-ph].

[56] M. Kramer et al., *Supersymmetry Production Cross Sections in pp Collisions at* $\sqrt{s} = 7$ *TeV* (2012), arXiv: 1206.2892 [hep-ph].

[57] P. Nason, *A New Method for Combining NLO QCD with Shower Monte Carlo Algorithms*, J. High Energy Phys. **0411** (2004) 040, arXiv: hep-ph/0409146 [hep-ph].

[58] S. Frixione, P. Nason, and C. Oleari, *Matching NLO QCD Computations with Parton Shower Simulations: the POWHEG Method*, J. High Energy Phys. **0711** (2007) 070, arXiv: 0709.2092 [hep-ph].

[59] S. Alioli et al., *A General Framework for Implementing NLO Calculations in Shower Monte Carlo Programs: the POWHEG BOX*, J. High Energy Phys. **1006** (2010) 043, arXiv: 1002.2581 [hep-ph].

[60] S. Frixione, P. Nason, and G. Ridolfi, *A Positive-Weight Next-to-Leading-Order Monte Carlo for Heavy Flavour Hadroproduction*, J. High Energy Phys. **0709** (2007) 126, arXiv: 0707.3088 [hep-ph].

[61] ATLAS Collaboration, *Measurements of Top Quark Pair Relative Differential Cross-Sections with ATLAS in pp Collisions at* $\sqrt{s} = 7$ *TeV*, Eur. Phys. J. **C73**.1 (2013) 2261, arXiv: 1207.5644 [hep-ex].

[62] ATLAS Collaboration, *Measurements of Normalized Differential Cross Sections for* $t\bar{t}$ *Production in pp Collisions at* $\sqrt{s} = 7$ *TeV Using the ATLAS Detector*, Phys. Rev. **D90**.7 (2014) 072004, arXiv: 1407.0371 [hep-ex].

[63] S. Alioli et al., *NLO Single-Top Production Matched with Shower in POWHEG: s- and t-Channel Contributions*, J. High Energy Phys. **0909** (2009) 111, arXiv: 0907.4076 [hep-ph].

[64] B. P. Kersevan and E. Richter-Was, *The Monte Carlo Event Generator AcerMC Versions 2.0 to 3.8 with Interfaces to PYTHIA 6.4, HERWIG 6.5 and ARIADNE 4.1*, Comput. Phys. Commun. **184** (2013) 919–985, arXiv: hep-ph/0405247 [hep-ph].

[65] ATLAS Collaboration, *Improved Luminosity Determination in pp Collisions at* $\sqrt{s} = 7$ *TeV Using the ATLAS Detector at the LHC*, Eur. Phys. J. **C73**.8 (2013) 2518, arXiv: 1302.4393 [hep-ex].

[66] ATLAS Collaboration, *Electron and photon energy calibration with the ATLAS detector using LHC Run 1 data*, Eur. Phys. J. **C74**.10 (2014) 3071, arXiv: 1407.5063 [hep-ex].

[67] ATLAS Collaboration, *Measurement of the Muon Reconstruction Performance of the ATLAS Detector Using 2011 and 2012 LHC Proton-Proton Collision Data*, Eur. Phys. J. **C74**.11 (2014) 3130, arXiv: 1407.3935 [hep-ex].

[68] M. Cacciari, G. P. Salam, and G. Soyez, *The Anti-*k_t *Jet Clustering Algorithm*, J. High Energy Phys. **04** (2008) 063, arXiv: 0802.1189 [hep-ph].

[69] M. Cacciari and G. P. Salam, *Dispelling the* N^3 *Myth for the* k_t *Jet-Finder*, Phys. Lett. B **641** (2006) 57–61, arXiv: hep-ph/0512210.

[70] ATLAS Collaboration, *Jet Energy Measurement with the ATLAS Detector in Proton-Proton Collisions at* $\sqrt{s} = 7$ *TeV*, Eur. Phys. J. **C 73** (2013) 2304, arXiv: 1112.6426 [hep-ex].

[71] ATLAS Collaboration, *Single Hadron Response Measurement and Calorimeter Jet Energy Scale Uncertainty with the ATLAS Detector at the LHC*, Eur.Phys.J. **C73**.3 (2013) 2305, arXiv: 1203.1302 [hep-ex].

[72] M. Cacciari and G. P. Salam, *Pileup Subtraction Using Jet Areas*, Phys. Lett. **B659** (2008) 119–126, arXiv: 0707.1378 [hep-ph].

[73] ATLAS Collaboration, *Calibration of b-Tagging Using Dileptonic Top Pair Events in a Combinatorial Likelihood Approach with the ATLAS Experiment*, Report No. ATLAS-CONF-2014-004 (2014), URL: https://cds.cern.ch/record/1664335.

[74] ATLAS Collaboration, *Calibration of the Performance of b-Tagging for c and Light-Flavour Jets in the 2012 ATLAS Data*, Report No. ATLAS-CONF-2014-046 (2014), URL: https://cds.cern.ch/record/1741020.

[75] ATLAS Collaboration, *Performance of Missing Transverse Momentum Reconstruction in ATLAS Studied in Proton-Proton Collisions Recorded in 2012 at 8 TeV*, Report No. ATLAS-CONF-2013-082 (2013), URL: https://cds.cern.ch/record/1570993.

[76] M. Baak et al., *HistFitter Software Framework for Statistical Data Analysis* (2014), arXiv: 1410.1280 [hep-ex].

Auxiliary material

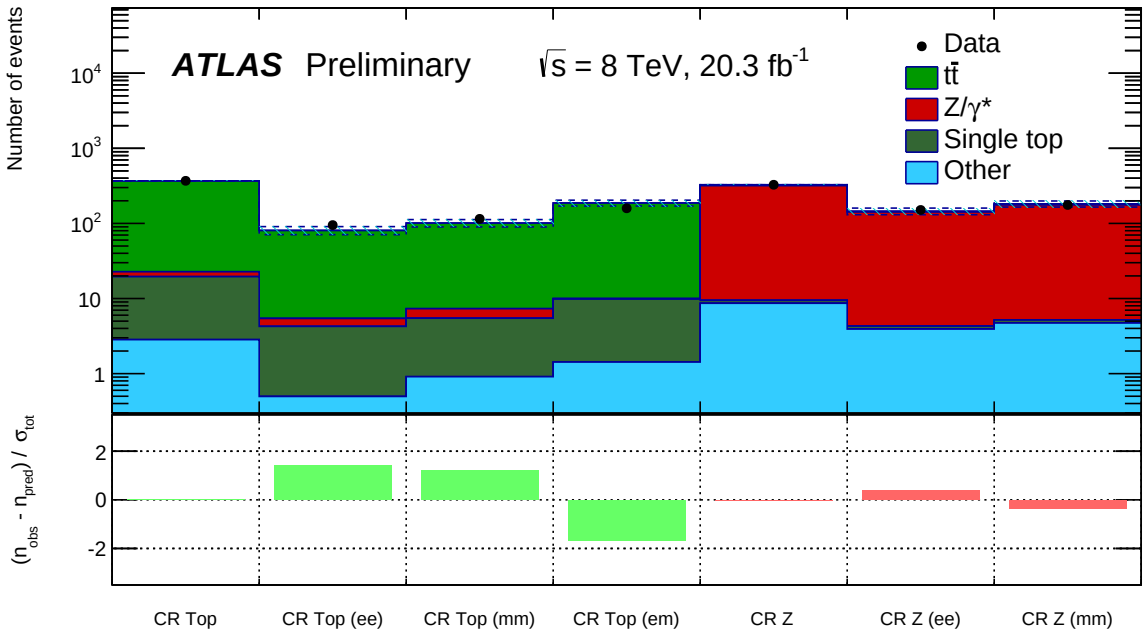

Figure 10: The top of this plot shows the number of observed and expected events in the CRs, and broken down by flavor channel. The uncertainty band includes the statistical uncertainty as well as the systematic uncertainty (described in Section 7. The bottom of the plot shows the deviation of that channel's prediction from the observed number of events divided by the uncertainty on the prediction. The normalization of the background yields are determined by fitting the $t\bar{t}$ and Z/γ^*+jets backgrounds to the observed data in the two CRs. As a result, the observed and predicted yields in the full Top CR and Z CR are equal.

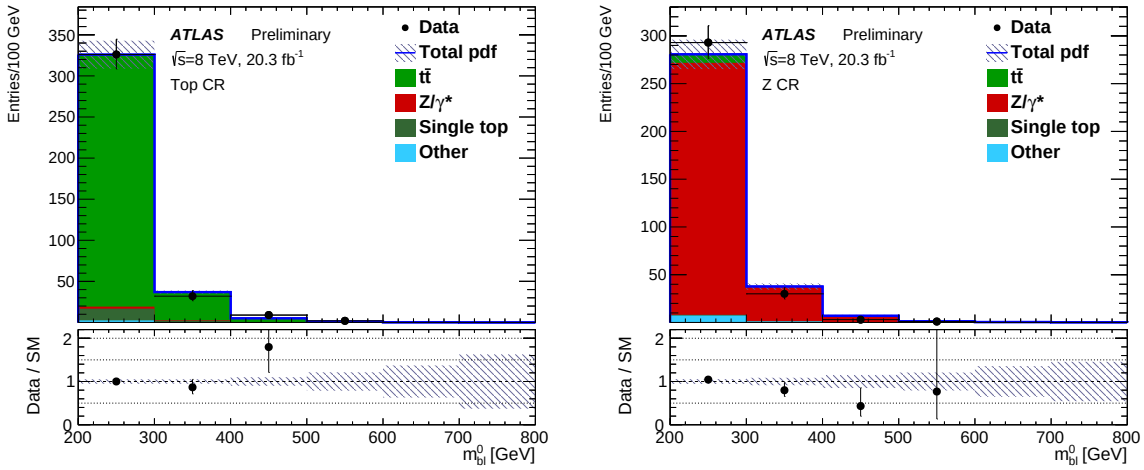

Figure 11: The $m^0_{b\ell}$ distribution in Top CR (left) and Z CR (right). The Standard Model background prediction is shown after setting the normalization of the $t\bar{t}$ and Z/γ^*+jets backgrounds based on the observed data in the CRs. The hashed bands show the uncertainty on the fitted background prediction including all statistical and systematics uncertainties. The bottom of each plot shows the ratio of the observed data to the Standard Model background prediction.

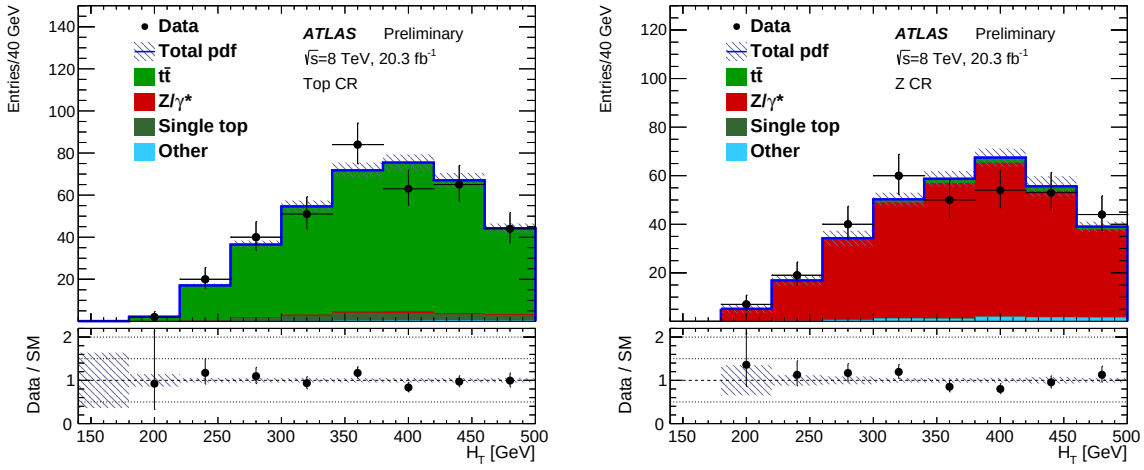

Figure 12: The H_{T} distribution in Top CR (left) and Z CR (right). The Standard Model background prediction is shown after setting the normalization of the $t\bar{t}$ and Z/γ^*+jets backgrounds based on the observed data in the CRs. The hashed bands show the uncertainty on the fitted background prediction including all statistical and systematics uncertainties. The bottom of each plot shows the ratio of the observed data to the Standard Model background prediction.

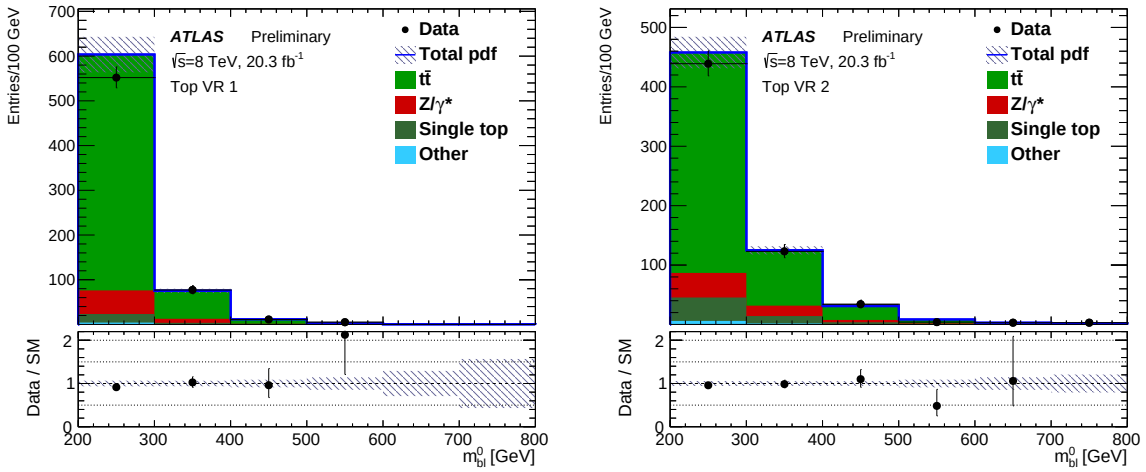

Figure 13: The $m^0_{b\ell}$ distribution in Top VR 1 (left) and Top VR 2 (right). The Standard Model background prediction is shown after setting the normalization of the $t\bar{t}$ and Z/γ^*+jets backgrounds based on the observed data in the CRs. The hashed bands show the uncertainty on the fitted background prediction including all statistical and systematics uncertainties. The bottom of each plot shows the ratio of the observed data to the Standard Model background prediction.

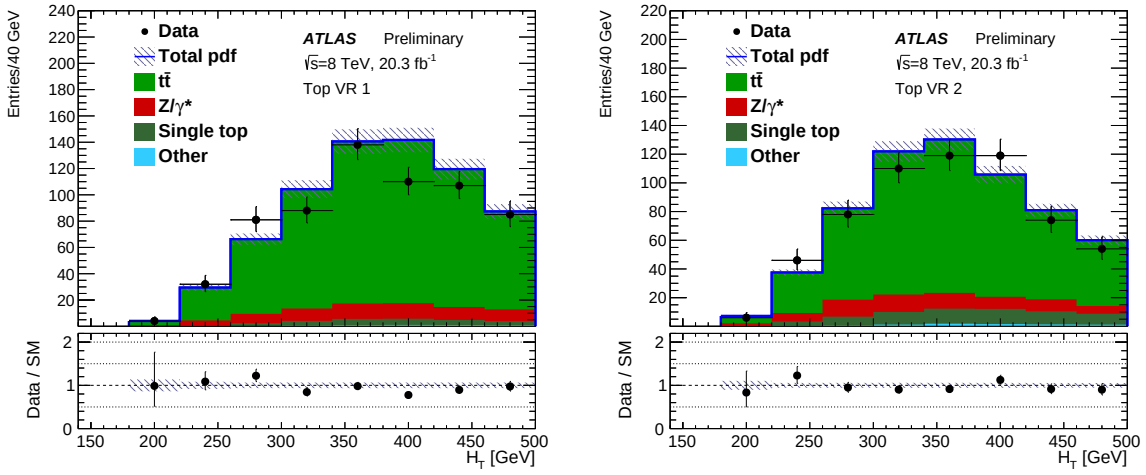

Figure 14: The H_{T} distribution in Top VR 1 (left) and Top VR 2 (right). The Standard Model background prediction is shown after setting the normalization of the $t\bar{t}$ and Z/γ^*+jets backgrounds based on the observed data in the CRs. The hashed bands show the uncertainty on the fitted background prediction including all statistical and systematics uncertainties. The bottom of each plot shows the ratio of the observed data to the Standard Model background prediction.

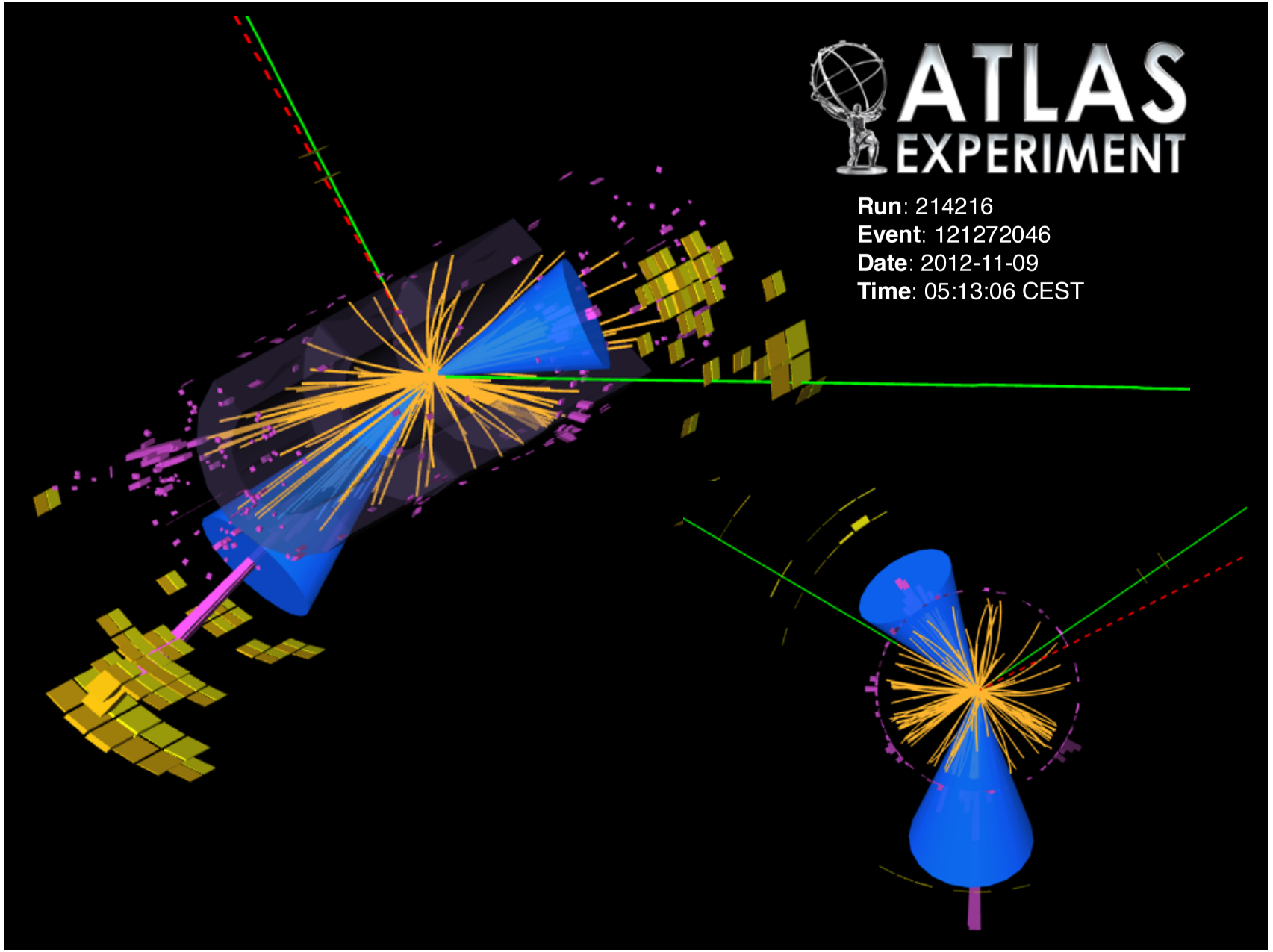

Figure 15: Event display for one of the observed events passing the signal region criteria. This event passes the SR 400 selection, with $m^0_{b\ell}$ = 558 GeV.

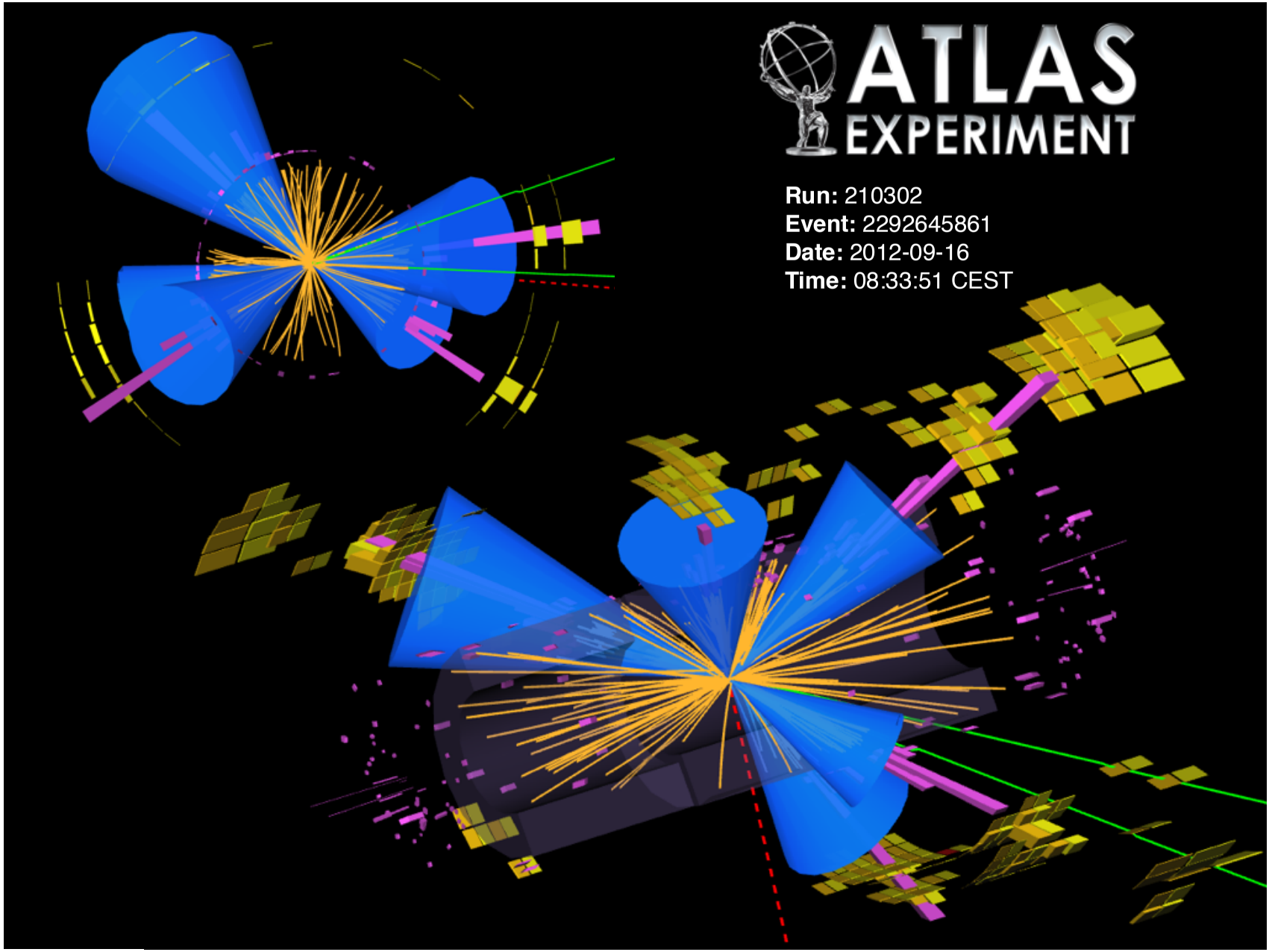

Figure 16: Event display for one of the observed events passing the signal region criteria. This event passes both the SR 400 and SR 600 selections, with $m^0_{b\ell} = 686$ GeV.